Structural boundary and deep contact relationship between the Yangtze and Cathaysia Blocks from crustal thickness gradients

Rubing Han[1], Dinghui Yang[1]*, Qiusheng Li[2]*, Wei Fu[3], Gaohua Zhu[4], Hongshuang Zhang[2], Hao Chen[5] and Yongzhi Cheng[2]

[1]Department of Mathematical Sciences, Tsinghua University, Beijing, China, [2]Key Laboratory of Deep-Earth Dynamics of Ministry of Natural Resources, Institute of Geology, Chinese Academy of Geological Sciences, Beijing, China, [3]College of Transportation Engineering, Nanjing Tech University, Nanjing, China, [4]CAS Key Laboratory of Marine Geology and Environment, Center for Ocean Mega-Science, Institute of Oceanology, Chinese Academy of Sciences, Qingdao, China, [5]School of Geophysics and Measurement-Control Technology, East China University of Technology, Nanchang, China

The deep boundary and contact relationship between the Yangtze and Cathaysia Blocks (the major tectonic units of the Southern China Block), as well as the tectonic attributes of the Jiangnan Orogenic Belt, have remained unknown or controversial. Using data recorded by 128 portable broadband stations and 96 permanent stations, we obtained high-resolution images of crustal thickness and Poisson's ratio in the study area. The influences of crustal anisotropy and inclined interface were eliminated by using the newly proposed receiver function H−κ−c stacking method. We then used a gradient analysis method to obtain crustal thickness gradients at the boundary of the Yangtze and Cathaysia Blocks for the first time. Our results reveal that the crustal thickness varies from >38 km in the Qinling−Dabie Orogenic Belt to <30 km east of the Tanlu Fault and Cathaysia Block. Areas with high Poisson's ratios (>0.27) are concentrated on the flanks of the deep fault zone and the continental margin of the study area; those with low Poisson's ratios (<0.23) are concentrated in the Jiangnan Orogenic Belt. Large crustal thickness gradients are found beneath the eastern part of the Jiujiang−Shitai buried fault (>5 km/°). Combined with the velocity structure and discontinuity characteristics at different depths, these findings suggest that the Jiujiang−Shitai fault may constitute a deep tectonic boundary dividing the Yangtze and Cathaysia Blocks on the lithospheric scale. Moreover, our results support that the Cathaysia Block subducted northwest-ward toward the southeastern margin of the Yangtze Block in the Neoproterozoic, and that the Jiujiang−Shitai buried fault and Jiangshan−Shaoxing fault are the deep and shallow crustal contact boundaries of the two Blocks, respectively; that is, the Yangtze Block overlaps the Cathaysia Block.

Introduction

Since the Neoproterozoic, the South China Block has experienced one of the most complex geological evolution processes worldwide, including collision collage, cleavage, destruction, and reconstruction (Shu, 2012; Zhang et al., 2012; Zhang et al., 2013). South China mainly consists of the Yangtze Block (YB), Cathaysia Block (CB), and the northeast-by-east (NEE)-trending Jiangnan Orogenic Belt (JOB) (Li et al., 2003; Charvet, 2013) (Figure 1). As important parts of South China, the YB and CB exhibit obvious differences in crustal composition and tectonic history. The YB is generally regarded as an Archean craton, and its basement, which is outcropped in its western part, is mainly composed of Archean to Proterozoic rocks (Qiu et al., 2000; Jiao et al., 2009). In comparison, the CB in the southeast is relatively young and consists mainly of Neoproterozoic basement and early Paleozoic sedimentary cover (Wang et al., 2007). The JOB (also known as the "Jinning Orogenic Belt" or "Sibao Orogenic Belt") is a linear uplift between the YB and CB. Constituting a set of Neoproterozoic trench-arc-basin assemblages, it is the product of collision–collage between the two Blocks (Zhang et al., 2021). The main part of the JOB is a large, NW-trending thrust fault–fold arc structural system; the inner deformation core comprises a Proterozoic structural uplift

belt that is asymmetrical and fan-shaped and derives from the Middle and Late Indosinian to Yanshan periods (Li et al., 2016; Shu et al., 2019). Identifying and analyzing the boundary and collage evolution of the YB and CB is important for the study of tectonic division, magmatic mineralization, and basic geological theory in South China (Shu, 2012). However, owing to the strong alteration of tectonic activities since the Mesozoic and limited data resolution, the deep boundary and contact relationship between the two Blocks, as well as the tectonic attributes and deep dynamic processes of the JOB, remain controversial.

The Jiangshan–Shaoxing fault is widely considered to constitute the boundary between the YB and CB, and the southern boundary of the JOB based on petrology, geochronology, geochemistry, geophysics, and isotope data (e.g., Li and Li, 2003; Li et al., 2009; Cawood et al., 2013; Zhang et al., 2015). However, the location of the northern boundary of the JOB has remained unclear owing to poor exposure of Precambrian lithologies. Knowledge of the crustal structure and its various horizontal rates would provide critical evidence for block-boundary identification. Seismological method is one of the important means of obtaining high-resolution crustal structures. Previous active- and passive-source surveys have obtained the major crustal structural characteristics of South China, promoting the understanding
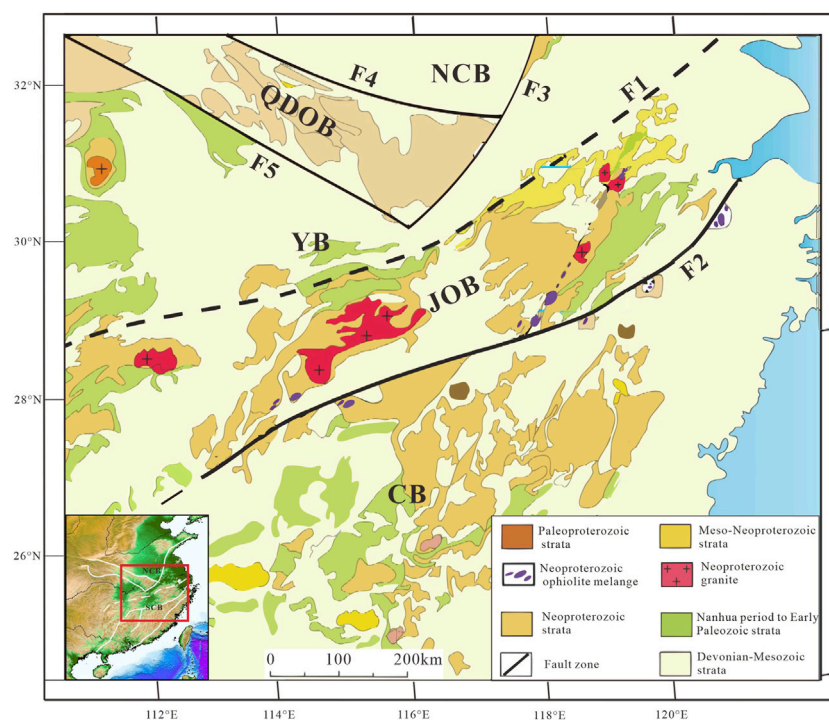
FIGURE 1
Simplified geological map of southeastern China, modified from Shu et al. (2019). NCB, North China Block; SCB, South China Block; YB, Yangtze Block; JOB, Jiangnan Orogenic Belt; QDOB, Qinling–Dabie Orogenic Belt; CB, Cathaysia Block; F1, Jiujiang–Shitai buried fault; F2, Jiangshan–Shaoxing fault; F3, Tanlu fault; F4, Xinyang–Shucheng fault; F5, Xiangfan–Guangji fault. The red rectangle in the illustration at the lower left corner indicates the study area.

FIGURE 2
Location map of seismic stations and teleseismic events (upper right corner) in Southeastern China. The background color map indicate the topography. The yellow triangles and squares represent the locations of the stations shown in Figure 3 and Figure 4 respectively. Blue solid lines represent CCP stacking section (see Figure 9C, modified from Ye et al., 2019). The triangle and black dots in the upper right corner indicate the center of the study area and teleseismic events, respectively. Main structural lines and fault lines are described in Shu et al. (2019).

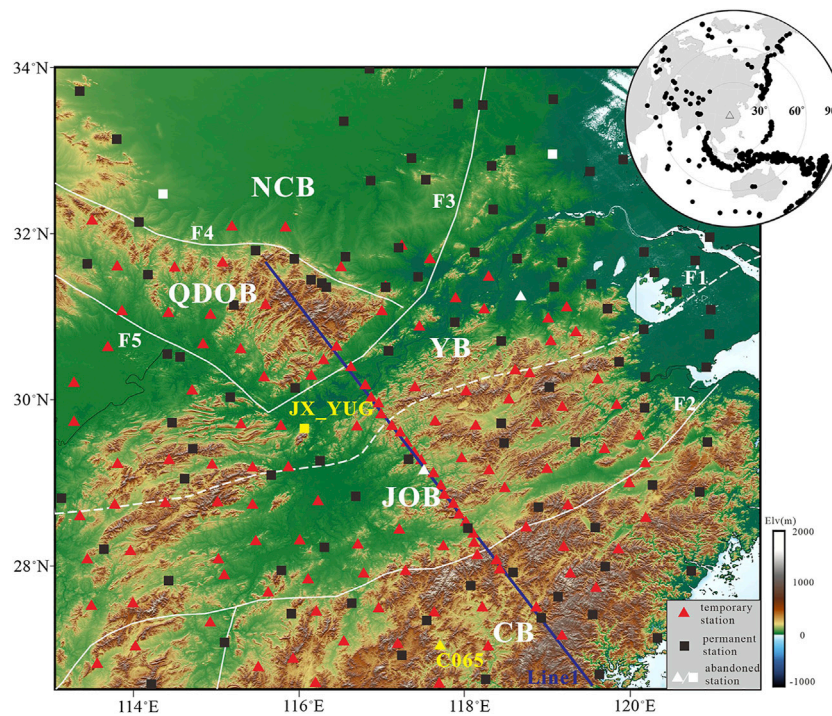of the deep structure and dynamic processes of this continent. Zhang et al. (2005) used wide-angle reflection/refraction data to identify velocity variations of the crustal and uppermost mantle on the two flanks of the Jiangshan–Shaoxing fault zone. The receiver function common conversion point (CCP) stacking results of Huang. (2013) show that the crustal thickness changes significantly on the two flanks of the Jiujiang–Shitai (Jiangnan) buried fault. These high-resolution seismic profile results provide abundant information on the boundary between the YB and CB, but it remains difficult to describe the deep boundaries and understand the relationship between the two blocks because of the limitations of the linear profile. Obvious differences in the lithospheric structure between the YB and CB have been revealed based on a two-dimensional (2-D) network of permanent stations in South China. The lithospheric thickness of the YB is approximately 200 km, the crustal thickness is approximately 45 km, and the crustal composition is mainly mafic. In comparison, a relatively thin lithosphere (approximately 80 km) and crust (approximately 30 km) are present in the CB, and the crustal composition is mainly felsic (Wei et al., 2016; Zhang et al., 2018; Shahzad et al., 2021; Zhang et al., 2021). Previous studies have suggested that the Jiujiang–Shitai fault may constitute the northern boundary of

the junction belt between the YB and CB, and have roughly described the spatial distribution of this buried fault zone (He et al., 2013; Guo and Gao, 2018; Zhang et al., 2019; Guo et al., 2019). However, owing to the sparse distribution of permanent stations and low resolution of the horizontal variation characteristics of the crustal structure obtained in previous studies, considerable uncertainty remains with regard to the location of the northern block boundary of the JOB.

Resolving this issue depends on the fine characterization of the 3-D Moho structure with high resolution in the junction belt. Dense seismic arrays can help to obtain high-resolution structural models of the Earth's interior. The organic combination of this acquisition scheme with permanent network-based observations can yield massive amounts of data, which allow substantial improvements in the spatial resolution of images of the Earth's interior. Among the multiple data processing methods, the receiver function method can effectively detect velocity discontinuities in the study area through rapid waveform stripping (Chen et al., 2022). In this study, we used data from 128 portable broadband stations and 96 permanent stations with complementary locations to provide enhanced coverage and dense sampling in the study area (Figure 2). The recently

proposed receiver function method of "corrected" crustal thickness–average crustal Vp/Vs ratio (H–κ–c) superposition (Li et al., 2019) was utilized to obtain high-resolution images of the crustal thickness and Poisson's ratio beneath the study area, following harmonic correction. With this framework, we applied a gradient analysis method that is sensitive to crustal thickness (or the Moho depth) to calculate the maximum horizontal gradient of the Moho which may represent the boundary of the YB and CB for the first time. This information provides key evidence for locating the boundary and identifying the directional trends of the main blocks in southeastern China.

Data and method

Data

A total of 128 temporary stations and 96 permanent stations were located in the study area (27°N–34°N, 113°E–123°E), which consists of five main tectonic units from north to south: the southern margin of the North China Block (NCB), the Qinling–Dabie Orogenic Belt (QDOB), the Lower Yangtze Block (YB), the Jiangnan Orogenic Belt (JOB), and the northeast region of the Cathaysia Block (CB). The temporary seismic stations used REFTEK-130 or Q330S+ data collectors, and CMG-3ESP (Band range, 60s-50 Hz) or CMG-3T (Band range, 120s-50 Hz) broadband seismometers with a sampling rate of 100 Hz. The data acquisition project of temporary stations was funded by China Geological Survey (CGS) and the fieldwork was finished cooperatively by Institute of Geology, Chinese Academy of Geological Sciences (IG of CAGS), Peking University (PKU), Nanjing University (NJU), Institute of Earthquake Forecasting of China earthquake Administration (IEF of CEA) and Institute of Geomechanics, Chinese Academy of Geological Sciences (IGM of CAGS) from July 2014 to December 2016, from which a total of 1,710 Gb data was recorded. The data of the permanent seismic stations were obtained from the Data Backup Centre for China Seismograph Network and recorded from January 2013 to December 2017 (Zheng et al., 2009).

According to standard processing flow (Liu et al., 1997; Wu and Zeng, 1998), we first removed the mean value, linear trend, *etc.* Then, we selected an earthquake catalogue corresponding to the study period from the United States Geological Survey (USGS), which contains 1,150 events with magnitudes greater than 5.5, and epicenter distances between 30° and 90°. Next, three-component waveforms (20 s before and 180 s after the first arrival P wave) were bandpass filtered by 0.05–2 Hz and rotated into Z-R-T coordinate to separate energy between the P wave and the conversions (Ps). We selected the data showing obvious first arrival of the P-wave without distortion, and employed time-domain iterative deconvolution to generate radial receiver

functions (Ligorría and Ammon, 1999) with a Gaussian coefficient of 3.0. A total of 28,710 receiver functions were chosen for further analysis. Figure 3 shows the receiver function arrangement of No. C065. Ps were identifiable on the delay time diagram at nearly 3–4 s after the first P-wave arrival, and the crustal multiples (PpPs, PpSs+PsPs) were also visible. Good back-azimuthal coverages and epicentral distances were also observed (Figure 3, right). A total of 23,415 receiver function records with obvious first arrivals and high signal-to-noise ratios were chosen for further processing.

H-κ-c method

Crustal thickness (H) can provide key evidence for block boundary identification and is a significant parameter for describing fluctuation of the Moho. The average crustal Vp/Vs ratio (κ) reflects the material composition, structure, and physical state of crust.
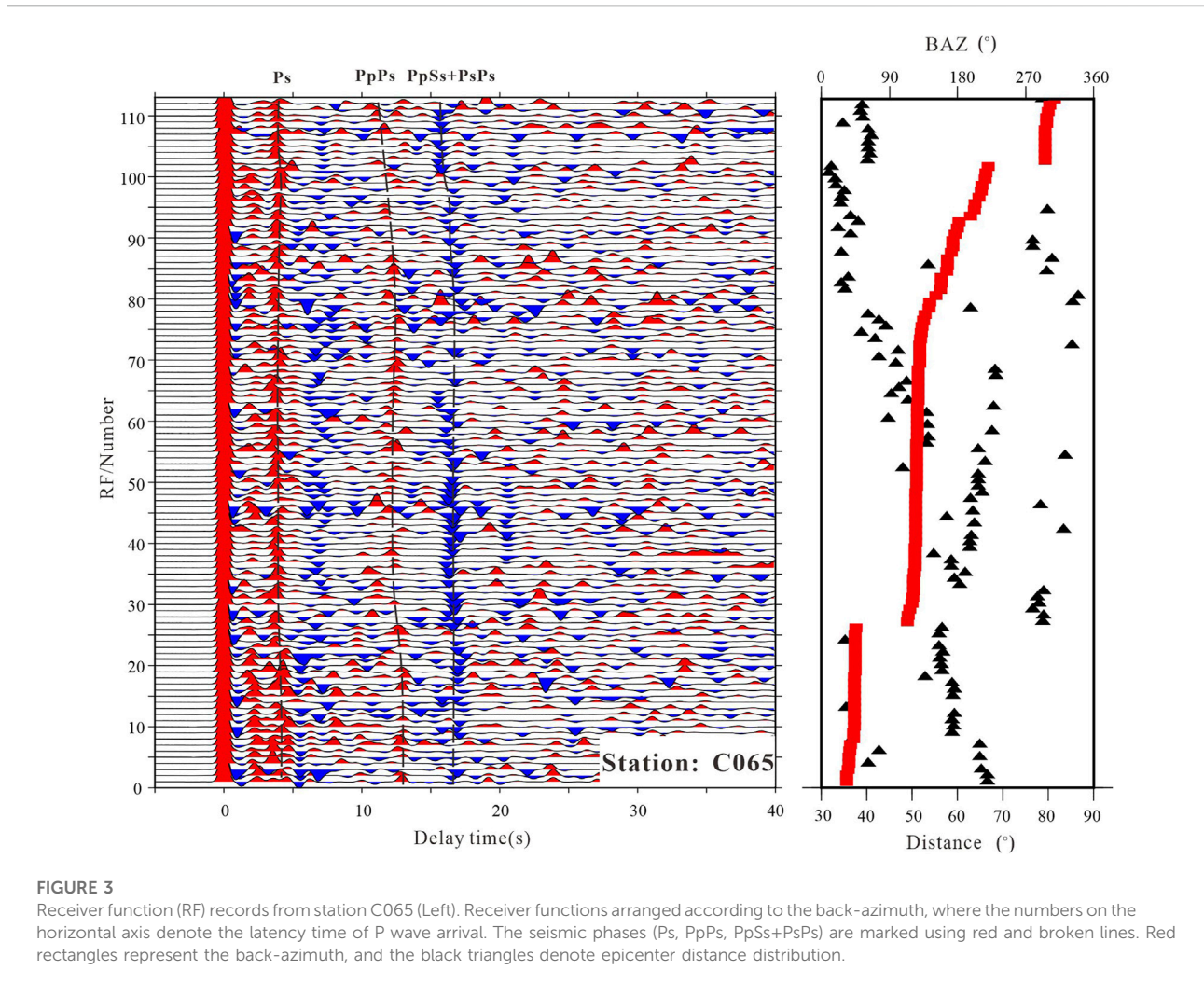
The receive function H–κ stacking method jointly constrains H and κ based on the arrival time relationship between the Moho surface converted wave Ps, crustal multiples PpPs (M1), PsPs+PpSs (M2), and direct P wave information (Zhu and Kanamori, 2000). With different combinations of H and κ, we calculated the theoretical arrival times of Ps, M1, and M2 based on the crustal average velocity of the P wave (Vp). According to the theoretical arrival time, the corresponding amplitude was obtained in the receiver function; then, the amplitude was weighted and summed to acquire the optimal estimation of the combination of H and italic. Compared with the direct P-wave, the calculation expressions for the travel time of Ps, M1 and M2 were as follows:

$$t_{ps} = H\left(\sqrt{\frac{\kappa^2}{V_P^2} - p^2} - \sqrt{\frac{1}{V_P^2} - p^2}\right)$$

$$t_{M1} = H\left(\sqrt{\frac{\kappa^2}{V_P^2} - p^2} + \sqrt{\frac{1}{V_P^2} - p^2}\right) \qquad (1)$$

$$t_{M2} = 2H\sqrt{\frac{\kappa^2}{V_P^2} - p^2}$$

where t_{ps}, t_{M1}, and t_{M2} represent the arrival time differences of Ps, M1, and M2, respectively, relative to the direct P wave under crustal thicknesses of H and κ. Vp represents the crustal average P-wave velocity and p represents the ray parameter. The weighted sum was calculated as follows:

$$S(H,\kappa) = w_1 r(t_{Ps}) + w_2 r(t_{M1}) - w_3 r(t_{M2}) \qquad (2)$$

where $r(t)$ is the amplitude of the receiver function; and w_1, w_2, and w_3 represent the proportions of Ps and crustal multiples in the superimposed energy, respectively. The Poisson's ratio (δ) can be obtained from its relationship with Vp/Vs (κ): $= 0.5 - \frac{1}{2(\kappa^2-1)}$. Mean square error estimation followed the

FIGURE 3
Receiver function (RF) records from station C065 (Left). Receiver functions arranged according to the back-azimuth, where the numbers on the horizontal axis denote the latency time of P wave arrival. The seismic phases (Ps, PpPs, PpSs+PsPs) are marked using red and broken lines. Red rectangles represent the back-azimuth, and the black triangles denote epicenter distance distribution.

method of Zhu and Kanamori (2000); that is, when $S(H, \kappa)$ reached the maximum value, it was Taylor expanded and take quadratic differentials for H and κ respectively. In particular:

$$\begin{cases} \sigma_H = 2\sigma_s \big/ \dfrac{\partial^2 s}{\partial H^2} \\[2mm] \sigma_k = 2\sigma_s \big/ \dfrac{\partial^2 s}{\partial \kappa^2} \end{cases} \tag{3}$$

mean-square deviations of H and κ, respectively. When the underground structure is relatively simple, the H–κ method can effectively constrain the crustal thickness and Vp/Vs ratio at the station because the arrival times of Ps and crustal multiples vary little with different azimuth angles. Nevertheless, when the crust has an obvious inclined interface (Lombardi et al., 2008) or anisotropic structures (Fang and Wu, 2009), the arrival times of the three phases vary considerably with the back-azimuth, causing the estimation results obtained using the H–κ method to deviate markedly from the real results, and even deviate from the normal range (Hammond, 2014). The inclined Moho surface

and inner crustal interface lead to variations of the arrival time of the Ps, M1, and M2 seismic phases with the back-azimuth, taking 360° as the period. S-wave azimuthal anisotropy leads to variation in the arrival time of the seismic phase with the back-azimuth, taking 180° as the period. Moreover, an inclined interface and S-wave azimuthal anisotropy change the polarity of the multi-wave seismic phase, thereby reducing the estimation of the useful seismic phase energy stacking upon H–κ calculation and causing the search results to deviate.

The H–κ–c method represents an improved, "corrected" H–κ technology proposed by Li et al. (2019) considering both the Moho surface inclination and azimuthal anisotropy structure. Basically, harmonic fitting is performed on the three phases to minimize the biases due to the dipping Moho and crustal anisotropy. At present, the H–κ–c method has been widely applied to receiver function imaging of crustal structures in China, elucidating many detailed characteristics of crustal structures (Zhang et al., 2020; Li et al., 2021; Han et al., 2022). In particular, the second-order harmonic equation $F(\theta)$

FIGURE 4
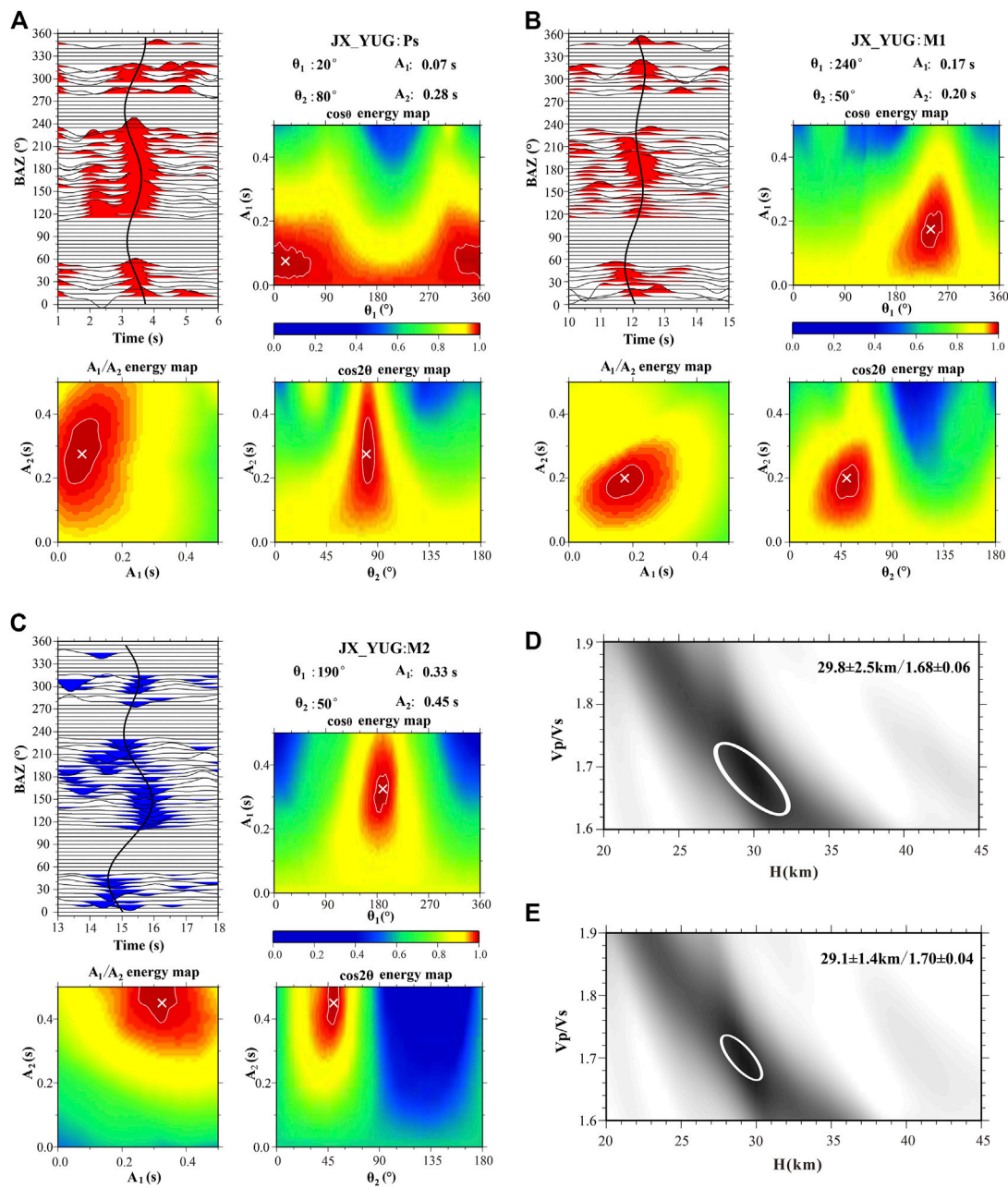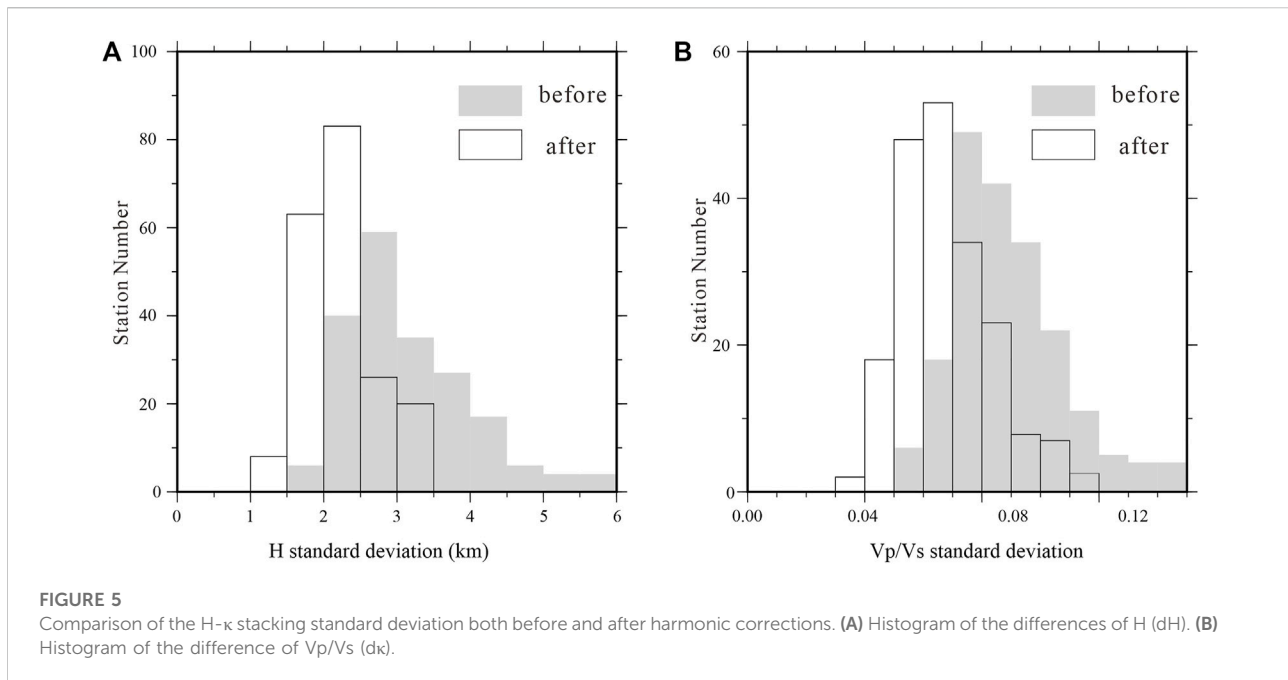Harmonic fitting of Ps **(A)**, M1 **(B)**, and M2 **(C)** for JX_YUG. The black lines represent the arrival times of Ps, M1, and M2 phases. The cross marks indicate the best solutions, and the 99% contours show the empirical uncertainty. H−κ domain energy maps are shown with weighting factors of 0.7/ 0.2/0.1 **(D)** in H−κ stacking and 0.6/0.3/0.1 **(E)** in H−κ−c stacking. H, κ, and their uncertainties (σH, σκ) are listed in the top right. The error ellipses with one standard deviation (Zhu and Kanamori, 2000) are marked with white circles.

is used to fit the variations of Ps and crustal multiples with the back-azimuth affected by the inclined interface and S-wave azimuthal anisotropy. The harmonic fitting equation is as follows:

$$F(\theta) = A_0 + A_1 \cos(\theta - \theta_1) - A_2 \cos 2(\theta - \theta_2) \qquad (4)$$

where $F(\theta)$ represents the arrival time of the Ps and crustal multiples as the back-azimuth (θ) changes, A_0 represents the center arrival time, and A_1, A_2, θ_1, and θ_2 represent the amplitude and phase of the first- and second-order changes, respectively. The harmonic correction is to find the optimal solution in the five-dimensional parameter ($dt=A_0-t_{ref}$, A_1, A_2, θ_1, θ_2) space,

FIGURE 5
Comparison of the H-κ stacking standard deviation both before and after harmonic corrections. **(A)** Histogram of the differences of H (dH). **(B)** Histogram of the difference of Vp/Vs (dκ).

where t_{ref} represents the arrival time of Ps calculated using the traditional H–κ stacking method, and the preliminary search range of each parameter is set as: dt: −1.0 to 1.0 s; A_1, A_2: 0–0.5 s; θ_1: 0–355°; θ_2: 0–175° (Li et al., 2019). A_1 and A_2 can be adjusted if the region is characterized by a larger interface inclination or greater anisotropic strength. In this study, the average crustal Vp (6.3 km/s) value was obtained from the deep seismic profiles (Zheng et al., 2003), and we set the search interval of crustal thickness (H) to be 20–50 km and the Poisson's ratio (κ) to be 1.5–2.0 according to the regional geological characteristics (He et al., 2013; Wei et al., 2016). The weighting factors of the three phases (Ps, M1, and M2) were adjusted from 0.7, 0.2, and 0.1, to 0.6, 0.3, and 0.1, respectively. The weighting of M1 was increased because the harmonic corrections enhanced the coherency of the M1 phase as well as the stacking energy, while the weighting of M2 remained because it was relatively weaker and more complicated.
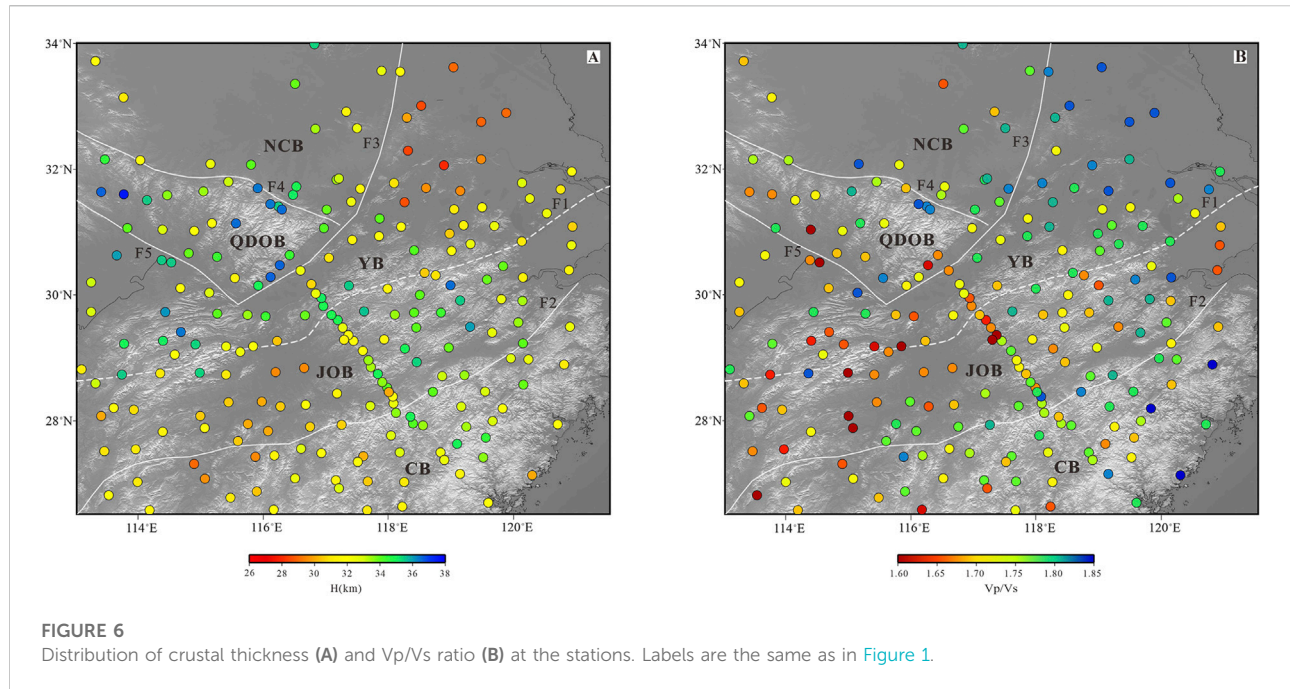
The detailed steps of the H–κ–c stacking method can be described as follows: 1) use the traditional H–κ method to obtain the reference arrival times t_{ref} of Ps, M1, and M2; 2) apply move-out corrections for all receiver functions to eliminate arrival times caused by different epicenter distances; 3) obtain the harmonic coefficients of the subsequent azimuth changes of Ps, M1, and M2 through harmonic fitting; and 4) use the harmonic parameters obtained in (3) to correct the corresponding Ps and crustal multiples, and apply traditional H–κ stacking again. As shown in Figure 4, the area of the one-sigma error ellipse decreased after harmonic correction. Overall, the standard deviations of H and κ are reduced from an average of ~3.50 km,

~0.08 to an average of ~2.0 km, ~0.06 (Figure 5). This validates the robustness of the H-κ-c method.

Gradient analysis method

In addition, to highlight the spatial distribution of the abrupt lateral Moho variations at the block boundary, we applied a technical strategy and method based on gradient analysis to obtain the first-order derivation of the crustal thickness value along the longitude and latitude directions in the spatial domain, and then conducted vector summation to obtain a "rate of change" distribution map (Xu et al., 2020). Compared with the traditional observation of the absolute value of the thickness, the gradient results provide more abundant information for the study of geological processes and have higher resolution along the block contact boundary. This is helpful in revealing local structural deformation characteristics that may be masked, and in further exploring geological issues such as the deep boundary division of lithospheric block units.

This analysis method requires 2-D imaging results with a large range and high resolution, and our new crustal thickness structure by the H–κ–c stacking method provides an apt basis for this analysis. The maximum horizontal gradient of the Moho is calculated as follows: 1) we applied an equally weighted spatial filter to the crustal thickness values with a filter radius of 30 km; 2) we calculated the first-order difference in the crustal thickness at each node along both the longitudinal and latitudinal directions; 3) we obtained the maximum horizontal gradient

FIGURE 6
Distribution of crustal thickness **(A)** and Vp/Vs ratio **(B)** at the stations. Labels are the same as in Figure 1.

of the Moho from vector summations of the longitudinal and latitudinal gradients.

Results

Crustal thickness and gradients characteristics

We obtained the crustal thickness (H), Vp/Vs ratio, and Poisson's ratio (κ) after harmonic corrections using the H–κ–c stacking technique; the results are shown in Figure 6 and Supplementary Table S1. We abandoned four stations, which are shown in Figure 2, owing to the negative influence of the quality and quantity of station records, site conditions, underground structures, *etc*. In addition, because 19 stations had back-azimuth gaps of >90°, the harmonic correction was void; therefore, H and κ were still calculated using the traditional H–κ method. The statistical results show that the crustal thickness in the study area varies from 28.0 to 37.6 km, with an average value of 32.6 km; the error range was 1.0–3.3 km, and the average error value was 2.2 km. The Vp/Vs ratio varied from 1.63 to 1.82, (average 1.73); the error range was 0.03–0.11, and the average error value was 0.06. The low-error estimates for each station also indicate that the calculation result is reliable; results with relatively large errors were concentrated in the northeast of Jiangsu Province, where the sedimentary layer is relatively thick.

Figure 7 shows the 2-D variation characteristics of the crustal thickness and Poisson's ratio in the study area. Overall, our results reveal that H and κ exhibited obvious zoning and blocking

characteristics. The variation from >38 km in the QDOB (the largest crustal thickness) to <30 km east of the Tanlu fault (the smallest crustal thickness) is consistent with the variation in the deep seismic sounding results (Deng et al., 2011; Xu et al., 2014). The resolution of the crustal thickness and Poisson's ratio was markedly improved with the substantial increase in seismic stations. The results further reveal that in the JOB and CB in the southern part of the study area, the crustal thickness generally does not exceed 32 km, whereas in high elevation areas, such as the Huangshan and Wuyishan, the crust is relatively thick (up to approximately 35 km).

Figure 7A illustrates the obvious difference in crustal thickness on the two flanks of the eastern part of the Jiujiang–Shitai buried fault (F1). Except for the relatively high elevation area in the eastern part of the JOB, the crust is relatively thick on the northwest side of F1, approximately 34 km, and relatively thin on the southeast side of F1, approximately 30 km. Figure 8 shows the distribution of the maximum horizontal gradient of the crustal thickness in the study region. A gradient zone with large lateral gradients is visible along the eastern part of the Jiujiang–Shitai buried fault (F1), with the gradient value >5 km/° (indicated by the red arrow), whereas no obvious change is observable along the Jiangshan–Shaoxing fault zone (F2), which is traditionally considered as the boundary between the YB and CB. In addition, the gradient results show that the eastern part of the QDOB is divided into several small blocks. As the deep boundary between the east and west of the Dabie Orogenic Belt, the Shangcheng–Macheng fault (F6) has obvious differences in rock assemblages, tectonic styles, and metallogenic backgrounds on the two flanks (Liu and Zhang,
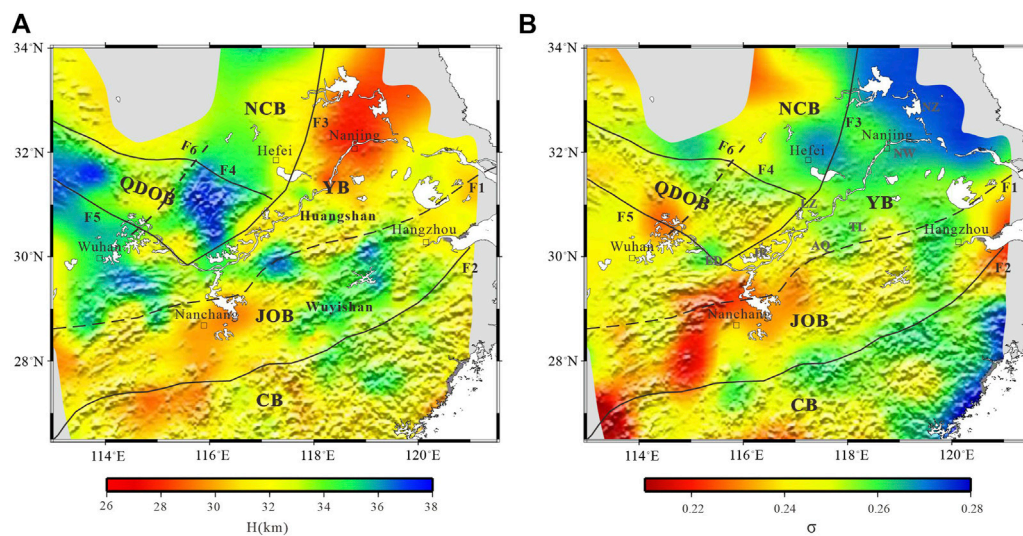
FIGURE 7
Two-dimensional distribution map of crustal thickness **(A)** and Poisson's ratio **(B)** in the study area. NZ, Ningzhen deposits; NW, Ningwu deposits; LZ, Luzong deposits; AQ, Anqing deposits; TL, Tongling deposits; JR, Jiurui deposits; ED, Southeastern Hubei deposits. F6, Shangcheng-Machang fault. Labels are the same as in Figure 1.
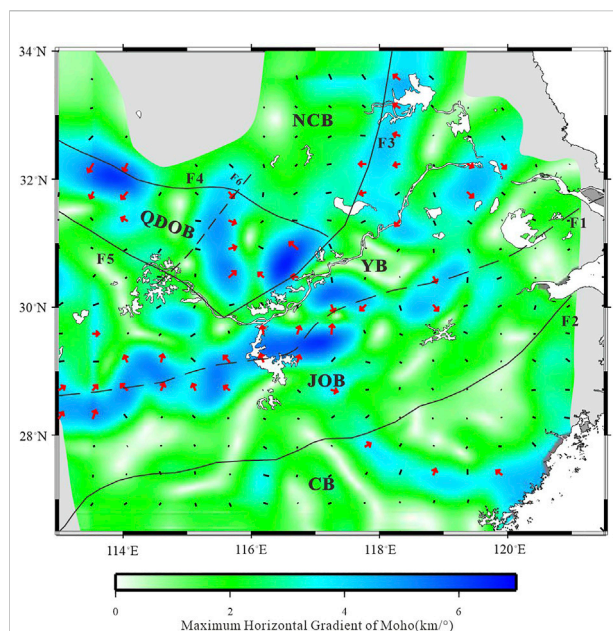

FIGURE 8
Maximum horizontal gradients of the crustal thickness. Short bars denote the directions of maximum gradients for every grid; red arrows show the grids with corresponding gradients >4 km/°. The direction indicated by the arrow indicates that the crustal thickness increases. Labels are the same as in Figure 1.

2013). The gradient results also show that the fault constitutes a deep boundary, and that the variation characteristics of crustal thickness are very clear, which is consistent with previous Pn tomography results (Gu et al., 2016; Yin et al., 2019). As shown in Figure 7A, east of the Tanlu fault (F3), at the site of the NCB and YB impact and bonding, the Moho depth is approximately 28 km, which is 3–5 km thinner than that of the surrounding structural units. The crustal thinning zone is distributed along the NE–SW direction and extends southward to the Jiujiang–Shitai buried fault (F1). The northern end cannot be clearly described as limited by the study area. The gradient results (Figure 8) more clearly describe the boundary of the crustal thinning zone (Shi et al., 2013; Xu et al., 2014).

Poisson's ratio variation

In general, the Poisson's ratio distribution in the study area shows obvious 2-D characteristics and a staggered alternating distribution (Figure 7B). Areas with high Poisson's ratios are concentrated on the two flanks of the Tanlu (F3) and Jiangshan–Shaoxing (F2) faults, as well as the southeast coastal area, with an average value of >0.27. In the bonding zone of the YB and CB, the Poisson's ratio shows obvious low-value distribution characteristics, with an average value of <0.23.

A negative correlation was observed between crustal thickness and Poisson's ratio in the crustal thinning zone on the east side of the Tanlu fault zone (F3), as shown in Figure 7B. In particular, five of the seven ore deposits in the Middle–Lower Yangtze Metallogenic Belt are located in the crustal thinning area (Figure 7B); moreover, over 200 other small ore deposits are also present (Lin et al., 2021), reflecting the close correlation between mineralization and the thinning of crustal thickness.

Discussion

Crustal structure and attribute characteristics

The crustal structure and Poisson's ratio characteristics represent seismological traces in the Earth following the long geological evolution process, which can be used to infer the dynamic mechanism and deformation process of evolution (Chen et al., 2022). Poisson's ratio reflects the rock properties of the crust and is sensitive to the material composition of the crust and subsequent tectonic deformation. Increase in mafic and decreases in quartz lead to an increase in the Poisson's ratio of the rock. Partial melting and an increase in the fluid composition of a two-phase medium also increase Poisson's ratio (Ji et al., 2009).

Existing seismic studies (Shi et al., 2013; Lü et al., 2014, 2015; Xu et al., 2014; Zhang et al., 2015; Zhang et al., 2021) have attributed crustal thinning and Poisson's ratio increases on the east side of F3 to the melting–assimilation–storage–homogenization (MASH) mineralization process (Hildreth and moorbath, 1988; Richards, 2003); in addition, many intermediate-acid intrusive rocks have similar geochemical characteristics to those of adakite rocks, which also directly indicates the existence of strong crust–mantle interaction in this area (Wang and Mo, 1995; Xu et al., 2002). The distribution of high Poisson's ratios (>0.27) is clearly related to large regional fault zones (such as the Tanlu fault). Wan and Zhao. (2012) attributed this relationship to the existence of structural fault-sphere detachment and an oceanic-continental transitional lithosphere. Deep faults provide a channel for magma under plating or ejection and determine the shape of magma differentiation, rise, and emplacement in the crust, which allows more basic magmatic materials to intrude into the crust and become enriched near the fault zone, and provides a good environment for the emplacement of metallogenic materials at shallow depths. This thermal convection and the injection of mantle thermal materials into the continental crust provide a direct driving force for shallow iron–copper polymetallic mineralization (Deng and Wu, 2001). The extension of F3 to the mantle has become a consensus in the geoscience community and is been supported by deep seismic soundings (Zhang et al., 2015; Liu et al., 2015). We speculate that the formation of the magma chamber was accompanied by the thinning of the crust thickness and the increase of Poisson's ratio. The magma rose to the shallow crust along the deep suture zone (such as F3), and large-scale magmatic activity broke out and a variety of deposits were formed on the shallow crust (Lü et al., 2014, 2015; Zhang et al., 2015).

In a tectonic compression environment, felsic rocks are more likely to form pushover structures or folds than mafic rocks under the same temperature and pressure, resulting in a decrease in the crustal velocity ratio with an increase in crustal thickness.

In addition, delamination reduces the thickness of some basic rocks in the lower crust, resulting in a decrease in the crustal Poisson's ratio. The Poisson's ratio of the middle part of the JOB is generally low, with an average value of <0.23, forming an obviously low Poisson's ratio belt between the northern and southern borders (i.e., Jiujiang–Shitai buried fault in the north and Jiangshan–Shaoxing fault in the south) (He et al., 2013; Guo et al., 2019). One explanation is that intra continental orogenic movement shortened and thickened the crust in the Mesozoic, with thickening mainly occurring in the upper crust. This multi-stage tectonic action caused the JOB to have a thick upper crust and a low crustal Poisson's ratio (Zhang et al., 2021). Another explanation is related to the crustal thickening under the Mesozoic compression background and the crustal thinning in the later extension background (Chen et al., 2022). The velocity structure obtained using previous wide-angle reflection/refraction seismic sounding data shows that the P-wave velocity of the lower crust varies from 6.2 to 6.6 km/s in the JOB, which is far less than the average velocity of the lower crust for the whole South China Block (Lin et al., 2021). According to geochemical and chronological studies, the South China continent should be dominated by thick crust (>45 km) before the Mesozoic (Zhu and Kanamori, 2000; Zhang et al., 2015). The latest results in this study show that the current average crustal thickness of JOB is about 30 km. All these provide further support for the thinning of the lower crust and reduction of the mafic composition.

Deep boundary between the YB and CB

It is difficult to clearly describe the characteristics of this sharp change in crustal thickness based on absolute thickness results. Blocks that have undergone different evolutionary histories or suffered different degrees of deformation leave records of thickness differences at the boundary during the assembling process; however, traces of structural deformation characteristics along the contact boundaries are often unclear owing to the long geological age and the influence of later reformation. It difficult to capture the precise position of the sharpest change in block thickness based only on the absolute value of Moho depth. Rather, such interpretation hinders the discrimination, identification, and further discussion of the deep contact relationship of the main block boundaries. The maximum horizontal gradients of crustal thickness obtained in this study, which clearly reveal the track of this buried fault (Figure 8). Our results show that the crustal thickness around the Jiangshan–Shaoxing fault (F2), which is traditionally considered as the boundary between the YB and CB (Zhang et al., 2005; Zhang et al., 2013; Zhang et al., 2018), does not vary significantly. However, a significant difference was observed in the crustal thickness variance on the two sides of the Jiujiang–Shitai buried fault (F1). We suggest that F1 may constitute the deep boundary
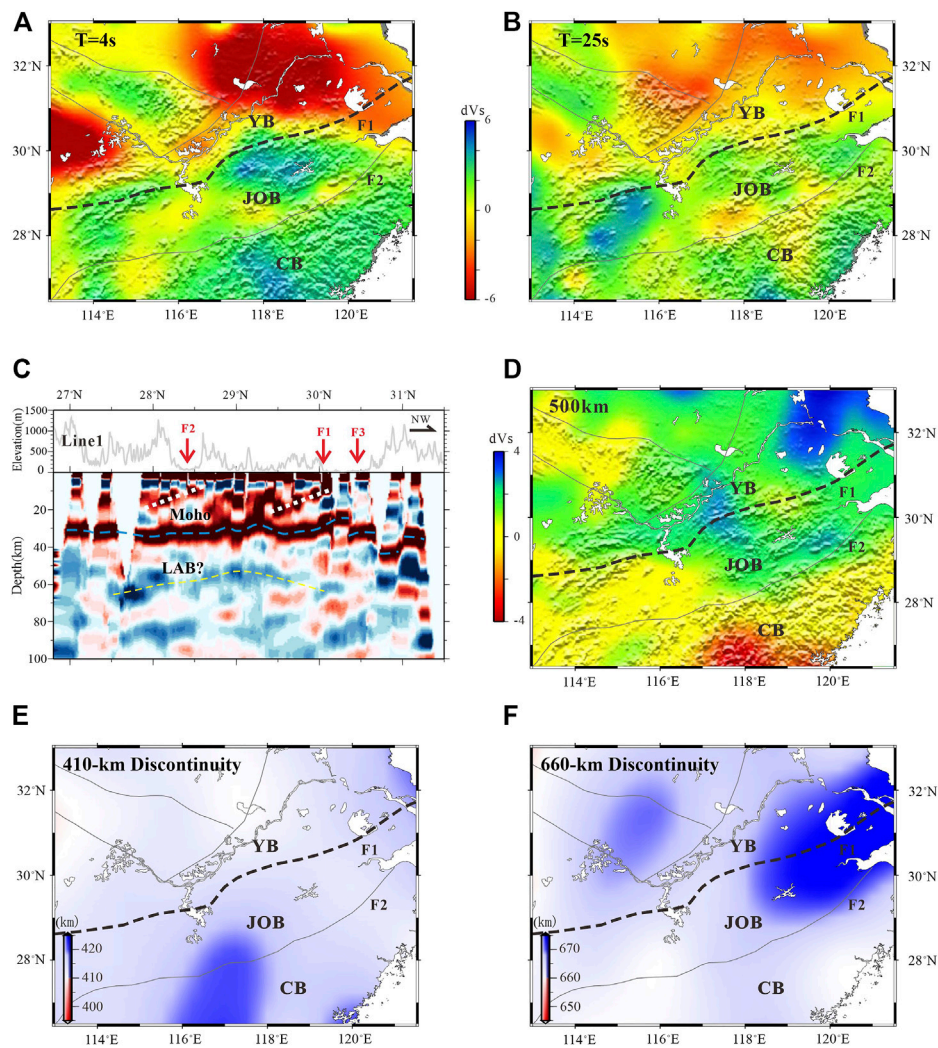
FIGURE 9
Rayleigh wave phase velocity perturbation at periods of 4 s **(A)** and 25 s **(B)** (Ma et al., 2022). Receiver function CCP stacking result **(C)** (Ye et al., 2019). S-wave velocity (Vs) tomography at the depth of 500 km **(D)** (Huang et al., 2021). Topography of the 410-km **(E)** and 660-km discontinuity **(F)** (Han et al., 2020). Labels are the same as in Figure 1.

between the YB and CB. The nature and scale of F2 have been widely recognized as first-order boundary faults between the YB and CB. The explanations for the insignificant abrupt change in the Moho depth on the two sides of F2 are as follows. First, the fault may extend to the base of the crust at a certain angle, resulting in the position of Moho break off not being imaged directly beneath the surface track of the fault (Zhang et al., 2013). Second, as a Neoproterozoic period bonding zone, the deep structure of F2 has been transformed by the subsequent extrusion and extension processes of the South China continent, resulting in relatively weak initial traces of the fault (Zhang et al., 2021). Specifically, the present Moho topography in South China should be the result of the reconstruction of the later tectonic events. Moho surface at the plate splicing part is

generally staggered and overlapped due to compression, which leads to unclear Moho imaging (Zhang et al., 2019; Shu et al., 2021). On the one hand, the seismic wave velocity and Poisson's ratio of the crust in the east of South China are relatively low, which is considered to be the result of the lower crustal delamination, which naturally makes the previously thickened crust tend to be average (Lin et al., 2021; Zhang et al., 2021); On the other hand, the subduction and retreat of the Mesozoic ancient Pacific plate resulted in the partial melting of the mantle wedge and the upwelling of the asthenosphere, which led to the overall extension of the crust and partial melting of the bottom (Huang and Zhao, 2006; Li and Li, 2007).

Based on our results, we infer that the central-eastern segment of F1 represents the deep boundary between the YB and CB,

whereas F2 is marked as the shallow boundary; that is, the southern margin of the YB overlaps the northern margin of the CB. The subduction direction of CB is believed to be NW based on the polarity of compressional tectonics of the JOB (Guo et al., 1989; Wang and Mo, 1995; Shu, 2012; Yao et al., 2019; Suo et al., 2020). This conclusion is supported by the results of recent ambient noise tomography experiments (Ma et al., 2022). Ma et al. (2022) clearly show that no obvious variation in S-wave velocity is apparent between the two sides of F2, whereas the central-eastern segment of F1 represents the transform boundary between low- and high-velocity during different periods of seismic waves (Figures 9A,B). Guo and Gao. (2018), Guo et al. (2019) also speculated that the JOB has a double-layer basement based on the differences in gravity, magnetic properties, and material composition in the crust. In the central–eastern segment of the JOB, F1 is the front edge of the lower basement of the CB and F2 is the upper basement Frontier of the YB. Moreover, the common conversion point (CCP) stacking result of receiver function also clearly shows that Moho is obviously staggered on both sides of the F1, and the inferred LAB seismic phase (Shan et al., 2021; Yang et al., 2021) also shows discontinuous characteristics (Figure 9C; Ye et al., 2019). The velocity imaging results revealed that the YB and CB show different velocity characteristics in the lithospheric mantle (Wang et al., 2018; Chen et al., 2022). S-wave receiver function showed that the lithosphere thickness in the lower YB and its adjacent regions is about 80–100 km, confirming the characteristics of lithosphere thinning (Zhang et al., 2019). Zhou et al. (2012) used the ambient noise and earthquake tomography to reveal that the west YB has a thicker lithospheric structure (~150 km or more), while the east YB is relatively thin (about 80 km), and the CB is the thinnest, only 60–70 km. However, previous studies have shown that the significant differences between tectonic units in South China are mainly characterized by the response of the crustal deformation (most of them limited within the crust) and magmatic activity, while the mantle lithosphere is entirely stretched during Mesozoic, and even at the block boundary, it will change smoothly. So it is difficult to use the differences of lithospheric structure for determining the minor or local-scale block boundary.

Tomography results reveal the presence of extensive low-velocity anomalies in the upper mantle of southeastern China to the north of F1, along with near-horizontal high-velocity bodies in the mantle transition zone (MTZ), which are similar to those in the North China and Northeast China Blocks. High-velocity anomalies are speculated to be caused by the Pacific subduction plate remaining in the MTZ (Huang and Zhao, 2006; Li and Van Der Hilst, 2010; Huang et al., 2014; Jiang et al., 2021). However, the MTZ in the CB, south of F1, showed no obvious high-velocity anomalies (Figure 9D; Li and Van Der Hilst, 2010; Huang et al., 2021). Moreover, according to a recent 3-D fine structure of the MTZ derived from the receiver function, there is a mantle boundary at 29°N, and the structural characteristics on the

two sides are different (Han et al., 2020). Overall, the depth of the 660-km discontinuity declines in the northern study area, and the 410-km discontinuity in the south is partially depressed, accompanied by obvious differences in temperature and water content. The surface projection of the deep boundary (29°N) has good spatial correspondence with the location and strike of F1 (Figures 9E,F). Obvious structural differences of MTZ on the two sides of F1 indicate that the YB and CB above may have different deep mantle dynamic environments.

Amalgamation of the YB and CB

The South China plate has undergone a long and multi-stage process of crustal evolution and continental transformation and exhibits complex and diverse crustal material composition and structural characteristics. The magmatism and metamorphism of the South China plate have resulted in the formation of a complex tectonic pattern of multi-block integration and basin-mountain coupling. One possibility is that the JOB formed between the YB and CB during the Mesoproterozoic Sibao orogeny (1,100–1,000 Ma; Li et al., 2019). Alternatively, shortening and subduction between the YB and CB may have occurred in the Neoproterozoic (~800 Ma) along the Jiujiang–Shitai buried fault on the southeastern margin of the JOB (Shu, 2012; Yao et al., 2014). Furthermore, a third slab-arc model (Zhao et al., 2011) proposed that the CB subducted NW-ward beneath the YB and that the final assembly of these two blocks occurred at approximately 830 Ma according to the compressional tectonic direction of the JOB, which is supported by other study data (Zhang et al., 2015; Xu et al., 2015; Yao et al., 2019; Ma et al., 2022). Based on the slab-arc model and the maximum horizontal gradients of the crustal thickness revealed in this study, combined with the previous research results, the proposed process of amalgamation between the YB and CB since the Neoproterozoic is illustrated in Figure 10.

During the Neoproterozoic, the CB subducted toward the southeastern margin of the YB along the NW- direction and collided with the YB to form a relatively stable South China lithosphere structure, resulting in low greenschist facies metamorphic rocks, ductile shear deformation, and magmatic activity in the southeastern margin of the YB (Shu et al., 2021). The Jiujiang Ms 5.7 main earthquake in 2005 may be the NW trending Yangjishan-Wushan-Tongjiangling fault concealed in the Ruichang basin, and the focal mechanism solution shows a sinistral strike slip fault of reverse nature (Tang et al., 2018). However, due to the focus too shallow, Lü et al. (2008) pointed out that this earthquake mainly corresponds to some small-scale secondary faults, which cannot represent the structure and stress state of the whole main fault. In addition, F1 and F2 are affected by multiple geological tectonic movements in the later period, and only thrust structures remained to present. Therefore, it is difficult to accurately describe their properties with the focal mechanism of current earthquakes. Besides, the deep reflection
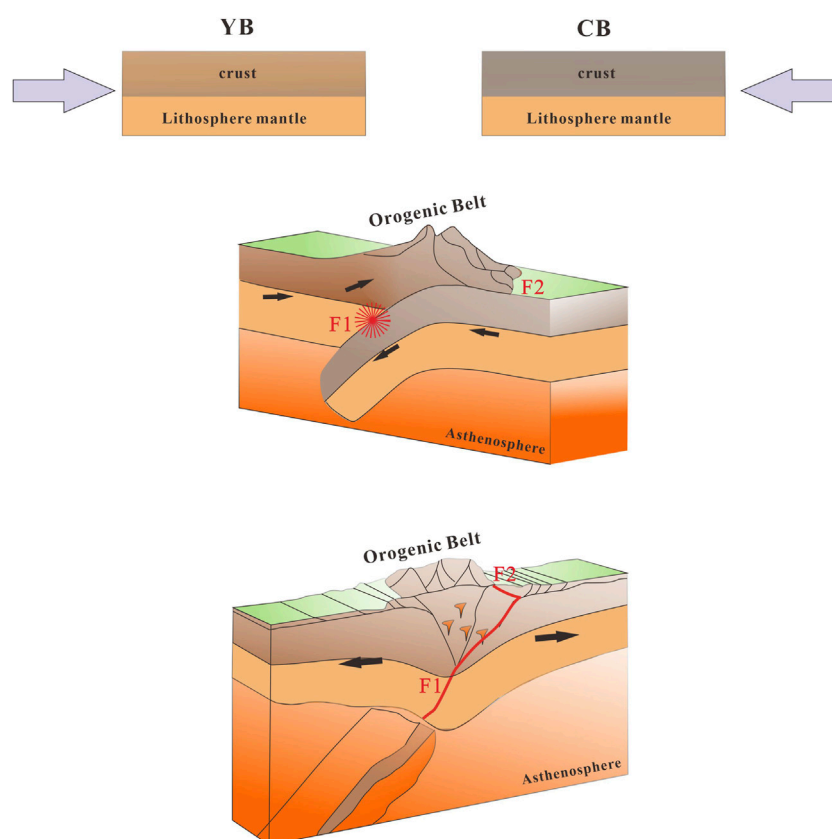
FIGURE 10
Subduction and amalgamation processes of suture zone between the YB and CB. This model describes the process of amalgamation between the YB and CB since the Neoproterozoic. The CB subducted northwest-ward toward the southeastern margin of the YB, and then underwent various geological processes, forming the current tectonic framework. Labels are the same as in Figure 1.

profile clearly shows the low-angle NE-SW thrust characteristics of several buried faults in the crust of eastern South China (Liang, 2014). The thrust feature in the middle and upper YB below the Jiangnan ancient suture can also be presented (Dong et al., 2015), indicating that this thrust fault in southeastern China is widespread. In addition, as shown in Figure 9C, the CCP result of the receiver function also records the thrust characteristics of F1 and F2 in the crust. The NE-trending Jiangnan Neoproterozoic arc Orogenic Belt was formed between the YB and CB, as supported by abundant geological and geophysical evidences related to collisional orogeny, such as strong compressive deformation of the strata, region-scale angular unconformity, ductile shear zone, arc migmatite associated with subduction, high-pressure gneiss, syn-collisional granites, and ophiolite mélange, representing ancient oceanic crust (Shu, 2012; Zhao et al., 2013; Chu et al., 2020). The eastern section of the Jiujiang–Shitai buried fault may represent the deep boundary (mantle-scale) between the CB and YB, whereas the Jiangshan–Shaoxing fault is the surface track, with the CB subducted beneath the YB.

Following collision, the South China Block underwent multiple extensional-compressional processes and metamorphic deformation events, including: Neoproterozoic (approximately 800–750 Ma) rifting events on a lithosphere scale (Shu, 2012; Zhang et al., 2012); early Paleozoic (approximately 460–400 Ma) large-scale metamorphic deformation and magmatic events affecting the middle and lower crust (Wang et al., 2012); early Mesozoic (approximately 260–200 Ma) tectonic-magmatic events characterized by thin-crust tectonics, thrust nappe, and large-scale peraluminous magmatism (Zhao et al., 2013; Li et al., 2017); and late Mesozoic back-arc extension and multi-stage and multi-type magmatic events controlled by the subduction of the Paleo–Pacific Plate (Huang and Zhao, 2006; Li and Li, 2007). The high potassium calc-alkaline granite formed in the late Yanshan period (142–67 Ma) has a higher Poisson's ratio (Zhou et al., 2006; Li et al., 2014). The increasing trend of the crustal Poisson's ratio from inland to coastal areas (Figure 7B) is related to the crustal evolution process since the Mesozoic in South China (i.e., from inland to coastal, the age distribution

trend of magmatic rocks is from old to new). The high Poisson's ratio implies the underplating of the deep mafic magma (Ye et al., 2013; Chen et al., 2022). All these tectonic events may have influenced the formation of the present tectonic pattern.

Conclusion

In this study, we investigated teleseismic P-wave receiver functions based on the dense broadband seismic array in plan view, and obtained high-resolution images of crustal thickness and Poisson's ratio in southeastern China that eliminated the influence of crustal S-wave azimuth anisotropy and inclined interface. Consequently, the deep boundary and contact relationship between the YB and CB could be evaluated for the first time based on the variation of the maximum horizontal gradients of the crustal thickness. In particular:

(1) Crustal thickness varies from >38 km in the QDOB to <30 km in the CB and east of the Tanlu fault. Regions with relatively high Poisson's ratios are concentrated on the two flanks of the deep fault zone and the continental margin of the study area (>0.27), whereas those with lower Poisson's ratios are concentrated in the JOB (<0.23).

(2) The depth of the Moho east of the Tanlu fault is approximately 28 km, which is 3–5 km thinner than the geological units on the east and west sides; the fault extends to the vicinity of the Jiujiang–Shitai fault in the south with a strike of SW to NE. Combined with other geological and geophysical data, we infer that the deep structural characteristics of the Tanlu fault are closely related to extensive mineralization.

(3) The eastern section of the Jiujiang–Shitai buried fault constitutes a sharp Moho gradient zone with a maximum horizontal gradient of crustal thickness of >5 km/°. Combined with the velocity structure and discontinuity surface characteristics at different depths, we consider that the Jiujiang–Shitai buried fault may represent the deep structural boundary dividing the YB and CB at the mantle scale.

(4) The subduction and amalgamation model is supported by our results, in which the CB subducted northwest beneath the southern margin of the YB during the Neoproterozoic. The Jiujiang–Shitai fault is considered as the northern boundary of the JOB, whereas the Jiangshan-Shaoxing fault is the southern boundary.

Data availability statement

The original contributions presented in the study are included in the article/Supplementary Material, further inquiries can be directed to the corresponding authors.

Author contributions

RH: writing—original draft. DY: funding, project administration, and review. QL: supervision, provided raw data, and review. WF: conceptualization, formal analysis. GZ: suggesting, investigation. HZ: data processing, methodology. HC: editing. YC: data curation, software.

Conflict of interest

The authors declare that the research was conducted in the absence of any commercial or financial relationships that could be construed as a potential conflict of interest.

Publisher's note

All claims expressed in this article are solely those of the authors and do not necessarily represent those of their affiliated organizations, or those of the publisher, the editors and the reviewers. Any product that may be evaluated in this article, or claim that may be made by its manufacturer, is not guaranteed or endorsed by the publisher.

Supplementary material

The Supplementary Material for this article can be found online at: https://www.frontiersin.org/articles/10.3389/feart.2022.1065782/full#supplementary-material

References

Cawood, P. A., Wang, Y., Xu, Y., and Zhao, G. (2013). Locating South China in rodinia and gondwana: A fragment of greater India lithosphere? *Geology* 41 (8), 903–906. doi:10.1130/G34395.1

Charvet, J. (2013). The neoproterozoic–early paleozoic tectonic evolution of the South China block: An overview. *J. Asian Earth Sci.* 74, 198–209. doi:10.1016/j.jseaes.2013.02.015

Chen, C., Lü, Q., Chen, L., Shi, D., Yan, J., and Ai, Y. (2022a). Crustal thickness and composition in the South China Block: Constraints from earthquake receiver function. *Sci. China Earth Sci.* 65 (4), 698–713. doi:10.1007/s11430-021-9858-x

Chen, L., Wang, X., Wang, X., Wei, Z., and Zhang, J. (2022b). Advances and perspectives for receiver function imaging of the Earth's internal discontinuities and velocity structures. *Rev. Geophys. Planet. Phys.* 53 (0), 1–22. doi:10.19975/j.dqyxx.2022-029

Chu, Y., Lin, W., Faure, M., Allen, M., and Feng, Z. (2020). Cretaceous exhumation of the triassic intracontinental xuefengshan belt: Delayed unroofing of an orogenic plateau across the South China block? *Tectonophysics* 793, 228592. doi:10.1016/j.tecto.2020.228592

Deng, J., and Wu, Z. (2001). Lithospheric thinning event in the lower Yangtze craton and Cu-Fe metallogenic belt in the middle and lower Yangtze River reaches. *Geol. Anhui* 11 (2), 86–91.

Deng, Y., Li, S., Fan, W., and Liu, J. (2011). Crustal structure beneath South China revealed by deep seismic soundings and its dynamics implications. *Chin. J. Geophys.* 54 (10), 2560–2574. doi:10.3969/j.issn.0001-5733.2011.10.013

Dong, S., Zhang, Y., Gao, R., Su, J., Liu, M., and Li, J. (2015). A possible buried paleoproterozoic collisional orogen beneath central South China:Evidence from seismic-reflection profiling. *Precambrian Res.* 264, 1–10. doi:10.1016/j.precamres.2015.04.003

Fang, L., and Wu, J. (2009). Effects of dipping boundaries and anisotropic media on receiver functions. *Prog. Geophys* 24 (1), 42–50.

Gu, Q., Ding, Z., Kang, Q., and Zhao, Q. (2016). Pn wave velocity and anisotropy in the middle-southern segment of the Tan-Lu fault zone and adjacent region. *Chin. J. Geophys.* 59 (2), 504–515. doi:10.6038/cjg20160210

Guo, L., and Gao, R. (2018). Potential-field evidence for the tectonic boundaries of the central and Western Jiangnan belt in South China. *Precambrian Res.* 309, 45–55. doi:10.1016/j.precamres.2017.01.028

Guo, L., Gao, R., Shi, L., Huang, Z., and Ma, Y. (2019). Crustal thickness and Poisson's ratios of South China revealed from joint inversion of receiver function and gravity data. *Earth Planet. Sci. Lett.* 510, 142–152. doi:10.1016/j.epsl.2018.12.039

Guo, L., Shi, Y., Lu, H., Ma, R., Dong, H., and Yang, S. (1989). The pre-Devonian tectonic patterns and evolution of South China. *J. Southeast Asian Earth Sci.* 3 (1-4), 87–93. doi:10.1016/0743-9547(89)90012-3

Hammond, J. (2014). Constraining melt geometries beneath the Afar Depression, Ethiopia from teleseismic receiver functions: The anisotropic H-κ stacking technique. *Geochem. Geophys. Geosyst.* 15 (4), 1316–1332. doi:10.1002/2013GC005186

Han, R., Li, Q., Huang, R., and Zhang, H. (2020). Detailed structure of mantle transition zone beneath southeastern China and its implications for thinning of the continental lithosphere. *Tectonophysics* 789, 228480. doi:10.1016/j.tecto.2020.228480

Han, R., Yang, D., Li, Q., Chen, H., Zhang, H., Ye, Z., et al. (2022). Crustal structure and anisotropy in the Lower Yangtze region and its metallogenic implications. *Front. Earth Sci.* 10, 849088. doi:10.3389/feart.2022.849088

He, C., Dong, S., Santosh, M., and Chen, X. (2013). Seismic evidence for a geosuture between the Yangtze and Cathaysia blocks, south China. *Sci. Rep.* 3 (1), 2200–2207. doi:10.1038/srep02200

Hildreth, W., and Moorbath, S. (1988). Crustal contributions to arc magmatism in the Andes of central Chile. *Contr. Mineral. Pet.* 98 (4), 455–489. doi:10.1007/BF00372365

Huang, H. (2013). The crustal and upper mantle structure and anisotropy beneath the lower Yangtze Craton and its adjacent regions. [dissertation/doctor's thesis]. Nanjing: Nanjing University.

Huang, J., and Zhao, D. (2006). High-resolution mantle tomography of China and surrounding regions. *J. Geophys. Res.* 111 (B9), B09305. doi:10.1029/2005JB004066

Huang, R., Xu, Y., Luo, Y., and Jiang, X. (2014). Mantle transition zone structure beneath Southeastern China and its implications for stagnant slab and water transportation in the mantle. *Pure Appl. Geophys.* 171 (9), 2129–2136. doi:10.1007/s00024-014-0837-4

Huang, Z., Gou, T., and Wang, L. (2021). P and S wave tomography of east-central China: Insight into past and present mantle dynamics. *Tectonophysics* 809, 228859. doi:10.1016/j.tecto.2021.228859

Ji, S., Wang, Q., and Salisbury, M. (2009). Composition and tectonic evolution of the Chinese continental crust constrained by Poisson's ratio. *Tectonophysics* 463, 15–30. doi:10.1016/j.tecto.2008.09.007

Jiang, G., Zhang, G., Zhao, D., Lü, Q., Shi, D., Li, H., et al. (2021). Mantle flow and dynamics beneath central-east China: New insights from P-wave anisotropic tomography. *JGR. Solid Earth* 126 (5), e2020JB020070. doi:10.1029/2020JB020070

Jiao, W., Wu, Y., Yang, S., Peng, M., and Wang, J. (2009). The oldest basement rock in the Yangtze Craton revealed by zircon U-Pb age and Hf isotope composition. *Sci. China Ser. D-Earth. Sci.* 52 (9), 1393–1399. doi:10.1007/s11430-009-0135-7

Li, C., and Van Der Hilst, R. D. (2010). Structure of the upper mantle and transition zone beneath Southeast Asia from traveltime tomography. *J. Geophys. Res.* 115 (B7), B07308. doi:10.1029/2009JB006882

Li, J., Song, X., Wang, P., and Zhu, L. (2019). A generalized H-κ method with harmonic corrections on Ps and its crustal multiples in receiver functions. *J. Geophys. Res. Solid Earth* 124 (4), 3782–3801. doi:10.1029/2018JB016356

Li, J., Wang, X., Zhang, F., Zhou, X., and Shu, X. (2016). A rhythmic source change of the Neoproterozoic basement meta-sedimentary sequences in the Jiangnan Orogen: Implications for tectonic evolution on the southeastern margin of the Yangtze Block. *Precambrian Res.* 280, 46–60. doi:10.1016/j.precamres.2016.04.012

Li, J., Zhang, Y., Zhao, G., Johnston, S., Dong, S., Koppers, A., et al. (2017). New insights into phanerozoic tectonics of South China: Early paleozoic sinistral and triassic dextral transpression in the east wuyishan and chencai domains, NE Cathaysia. *Tectonics* 36 (5), 819–853. doi:10.1002/2016TC004461

Li, W., Chen, Y., and Xu, Y. (2021). Crustal SiO_2 content of the Emeishan Large Igneous Province and its implications for magma volume and plumbing system. *Geochem., Geophys., Geosyst.* 22 (8), e2021GC009783. doi:10.1029/2021GC009783

Li, W., and Li, X. (2003). Adakitic granites within the NE jiangxi ophiolites, South China: Geochemical and Nd isotopic evidence. *Precambrian Res.* 122 (1-4), 29–44. doi:10.1016/s0301-9268(02)00206-1

Li, X., Kind, R., and Yuan, X. (2003). Seismic study of upper mantle and transition zone beneath hotspots. *Phys. Earth Planet. Interiors* 136 (1-2), 79–92. doi:10.1016/S0031-9201(03)00021-9

Li, X., Li, W., Li, Z., Lo, C., Wang, J., Ye, M., et al. (2009). Amalgamation between the Yangtze and Cathaysia blocks in SouthSouth China: Constraints from SHRIMP U–Pb zircon ages, geochemistry and Nd–Hf isotopes of the shuangxiwu volcanic rocks. *Precambrian Res.* 174 (1-2), 117–128. doi:10.1016/j.precamres.2009.07.004

Li, Y., Gao, M., and Wu, Q. (2014). Crustal thickness map of the Chinese mainland from teleseismic receiver functions. *Tectonophysics* 611, 51–60. doi:10.1016/j.tecto.2013.11.019

Li, Z., and Li, X. (2007). formation of the 1300-km-wide intracontinental orogen and postorogenic magmatic province in mesozoic South China: A flat-slab subduction model. *Geol.* 35 (2), 179–182. doi:10.1130/G23119A.1

Liang, F. (2014). Deep structure of the middle part in the middle and lower reaches of Yangtze river: Insights from reflection seismic data. [dissertation/doctor's thesis]. China: Chinese Academy of Geological Sciences.

Ligorría, J., and Ammon, C. (1999). Iterative deconvolution and receiver-function estimation. *Bull. Seismol. Soc. Am.* 89 (5), 1395–1400. doi:10.1785/BSSA0890051395

Lin, J., Xu, T., Cai, H., Lü, Q., Bai, Z., Deng, Y., et al. (2021). Crustal velocity structure of Cathaysia Block from an active-source seismic profile between Wanzai and Hui'an in SE China. *Tectonophysics* 811, 228874. doi:10.1016/j.tecto.2021.228874

Liu, B., Feng, S., Ji, J., Shi, J., Tan, Y., and Li, Y. (2015). Fine lithosphere structure beneath the middle-southern segment of the Tan-Lu fault zone. *Chin. J. Geophys.* 58 (5), 1610–1621. doi:10.6038/cjg20150513

Liu, Q., Rainer, K., and Li, S. (1997). The receiver functions at the stations of the Chinese Digital Seismic Network (CDSN) and their nonlinear inversion. *Chin. J. Geophys.* 3, 356–368.

Liu, S., and Zhang, G. (2013). Mesozoic basin development and its indication of collisional orogeny in the Dabie orogen. *Chin. Sci. Bull.* 58, 827–852. doi:10.1007/s11434-012-5503-6

Lombardi, D., Braunmiller, J., Kissling, E., and Giardini, D. (2008). Moho depth and Poisson's ratio in the Western-Central Alps from receiver functions. *Geophys. J. Int.* 173 (1), 249–264. doi:10.1111/j.1365-246X.2007.03706.x

Lü, J., Zheng, Y., Ni, S., and Gao, J. (2008). Focal mechanisms and seismogenic structures of the Ms5.7 and ms 4.8 jiujiang-ruichang earthquakes of nov. 26, 2005. *Chin. J. Geophys.* 2008 (01), 158–164.

Lü, Q., Dong, S., Shi, D., Tang, J., Jiang, G., Zhang, Y., et al. (2014). Lithosphere architecture and geodynamic model of middle and lower reaches of Yangtze metallogenic belt: A review from SinoProbe. *Acta Pet. Sin.* 30 (4), 889–906.

Lü, Q., Dong, S., Tang, J., Shi, D., and Chang, Y.SinProbe-03-CJ Group (2015). Multi-scale and integrated geophysical data revealing mineral systems and exploring for mineral deposits at depth: A synthesis from SinoProbe-03. *Chin. J. Geophys* 58 (12), 4319–4343. doi:10.6038/cjg20151201

Ma, J., Huang, J., and Fu, Y. (2022). Phase velocity tomography of Rayleigh and Love waves in the suture zone between the Yangtze and Cathaysia Blocks. *Chin. J. Geophys.* 65 (4), 1255–1270. doi:10.6038/cjg2022P0217

Qiu, Y., Gao, S., McNaughton, N., Groves, D., and Ling, W. (2000). First evidence of >3.2 Ga continental crust in the Yangtze craton of south China and its implications for Archean crustal evolution and Phanerozoic tectonics. *Geology* 28 (1), 11–14. doi:10.1130/0091-7613(2000)028<0011: feogcc>2.3.co;2

Richards, J. (2003). Tectono- magmatic precursors for porphyry Cu-(Mo-Au) deposit formation. *Econ. Geol.* 98, 1515–1533. doi:10.2113/gsecongeo.98.8.1515

Shahzad, S., Liu, J., Sun, Y., and Li, C. (2021). Crustal structure and deformation in southeastern China revealed by receiver functions. *J. Asian Earth Sci.* 221, 104937. doi:10.1016/j.jseaes.2021.104937

Shan, B., Zhou, W., and Xiao, Y. (2021). Lithospheric thermal and compositional structure of South China jointly inverted from multiple geophysical observations. *Sci. China Earth Sci.* 64 (1), 148–160. doi:10.1007/s11430-019-9661-4

Shi, D. N., Lü, Q. T., Xu, W. Y., Yan, J. Y., Zhao, J. H., Dong, S. W., et al. (2013). Crustal structure beneath the middle–lower Yangtze metallogenic belt in east China: Constraints from passive source seismic experiment on the mesozoic intra-continental mineralization. *Tectonophysics* 606, 48–59. doi:10.1016/j.tecto. 2013.01.012

Shu, L. (2012). An analysis of principal features of tectonic evolution in South China Block. *Geol. Bull. China* 31 (7), 1035–1053. doi:10.3969/j.issn.1671-2552. 2012.07.003

Shu, L., Wang, J., and Yao, J. (2019). Tectonic evolution of the eastern Jiangnan region, South China: New findings and implications on the assembly of the Rodinia supercontinent. *Precambrian Res.* 322, 42–65. doi:10.1016/j.precamres.2018.12.007

Shu, L., Yao, J., Wang, B., Faure, M., Charvet, J., and Chen, Y. (2021). Neoproterozoic plate tectonic process and Phanerozoic geodynamic evolution of the South China Block. *Earth. Sci. Rev.* 216, 103596. doi:10.1016/j.earscirev.2021. 103596

Suo, Y., Li, S., Cao, X., Wang, X., Somerville, I., Wang, G., et al. (2020). Mesozoic-cenozoic basin inversion and geodynamics in east China: A review. *Earth. Sci. Rev.* 210, 103357. doi:10.1016/j.earscirev.2020.103357

Tang, J., Lü, J., Zeng, X., Yang, Y., Zeng, W., and Duan, L. (2018). Characteristics of focal mechanisms and stress field in the border region of Jiujiang and Ruichang. *J. Geodesy Geodyn.* 38 (08), 791–795+827. doi:10.14075/j. jgg.2018.08.005

Wan, T., and Zhao, Q. (2012). The Genesis of tectono-magmatism in eastern China. *Sci. China Earth Sci.* 55 (3), 347–354. doi:10.1007/s11430-011-4361-4

Wang, H., and Mo, X. (1995). An outline of the tectonic evolution of China. *Episodes* 18 (1), 6–16. doi:10.18814/epiiugs/1995/v18i1.2/003

Wang, X., Li, Q., Zhang, H., and Guo, Chen. (2018). Study of P-wave velocity structure in upper mantle in eastern South China. *Glob. Geol.* 37 (02), 620–626. doi:10.3969/j.issn.1004-5589

Wang, X., Li, X., Li, Z., Li, Q., Tang, G., Gao, Y., et al. (2012). Episodic precambrian crust growth: Evidence from U–Pb ages and Hf–O isotopes of zircon in the nanhua basin, central south China. *Precambrian Res.* 222, 386–403. doi:10.1016/j.precamres.2011.06.001

Wang, Y., Fan, W., Sun, M., Liang, X., Zhang, Y., and Peng, T. (2007). Geochronological, geochemical and geothermal constraints on petrogenesis of the indosinian peraluminous granites in the South China block: A case study in the hunan province. *Lithos* 96 (3-4), 475–502. doi:10.1016/j.lithos.2006.11.010

Wei, Z., Chen, L., Li, Z., Ling, Y., and Li, J. (2016). Regional variation in Moho depth and Poisson's ratio beneath eastern China and its tectonic implications. *J. Asian Earth Sci.* 115, 308–320. doi:10.1016/j.jseaes.2015.10.010

Wessel, P., and Smith, W. (1998). New, improved version of generic mapping tools released. *Eos Trans. AGU.* 79 (47), 579. doi:10.1029/98EO00426

Wu, Q., and Zeng, R. (1998). The crustal structure of Qinghai-Xizang plateau inferred from broadband teleseismic waveform. *Chin. J. Geophys.* 14, (05), 669–679.

Xu, J., Shinjo, R., Defant, M., Wang, Q., and Rapp, R. (2002). Origin of mesozoic adakitic intrusive rocks in the ningzhen area of east China: Partial melting of delaminated lower continental crust? *Geol.* 30 (12), 1111–1114. doi:10.1130/0091-7613(2002)030<1111:oomair>2.0.co;2

Xu, M., Huang, Z., Wang, L., Xu, M., Zhang, Y., Mi, N., et al. (2020). Sharp lateral Moho variations across the SE Tibetan margin and their implications for plateau growth. *J. Geophys. Res. Solid Earth* 125 (5), e2019JB018117. doi:10.1029/ 2019JB018117

Xu, T., Zhang, Z., Tian, X., Liu, B., Bai, Z., Lü, Q., et al. (2014). Crustal structure beneath the Middle-Lower Yangtze metallogenic belt and its surrounding areas: Constraints from active source seismic experiment along the Lixin to Yixing profile in East China. *Acta Pet. Sin.* 30 (4), 918–930.

Xu, X., Li, Y., Tang, S., Xue, D., and Zhang, Z. (2015). Neoproterozoic to Early Paleozoic polyorogenic deformation in the southeastern margin of the Yangtze Block: Constraints from structural analysis and 40Ar/39Ar geochronology. *J. Asian Earth Sci.* 98, 141–151. doi:10.1016/j.jseaes.2014.11.015

Yang, X., Li, Y., Afonso, J., Yang, Y., and Zhang, A. (2021). Thermochemical state of the upper mantle beneath South China from multi-observable probabilistic inversion. *JGR. Solid Earth* 126 (5), e2020JB021114. doi:10.1029/2020JB021114

Yao, J., Cawood, P., Shu, L., and Zhao, G. (2019). Jiangnan orogen, South China: a~ 970–820 Ma rodinia margin accretionary belt. *Earth. Sci. Rev.* 196, 102872. doi:10.1016/j.earscirev.2019.05.016

Yao, J., Shu, L., Santosh, M., and Zhao, G. (2014). Neoproterozoic arc-Related mafic–ultramafic rocks and syn-collision granite from the Western segment of the jiangnan orogen, South China: Constraints on the neoproterozoic assembly of the Yangtze and Cathaysia blocks. *Precambrian Res.* 243, 39–62. doi:10.1016/j. precamres.2013.12.027

Ye, Z., Li, Q., Gao, R., Guan, Y., He, R., Wang, H., et al. (2013). Seismic receiver functions revealing crust and upper mantle structure beneath the continental margin of southeastern China. *Chin. J. Geophys.* 56 (9), 2947–2958. doi:10.6038/ cjg20130909

Ye, Z., Li, Q. S., Zhang, H. S., Li, J. T., Wang, X. R., Han, R. B., et al. (2019). Crustal and uppermost mantle structure across the Lower Yangtze region and its implications for the late Mesozoic magmatism and metallogenesis, eastern South China. *Phys. Earth Planet. Interiors* 297, 106324. doi:10.1016/j.pepi.2019.106324

Yin, W., Lei, J., Du, M., Yang, Y., Mi, Q., Lu, M., et al. (2019). Uppermost-mantle Pn velocity and anisotropic tomography of the Tanlu fault zone and adjacent areas. *Chin. J. Geophys.* 62 (11), 4227–4238. doi:10.6038/cjg2019M0672

Zhang, B., Bao, X., and Xu, Y. (2020). Distinct orogenic processes in the south- and north-central tien Shan from receiver functions. *Geophys. Res. Lett.* 47 (6), e2019GL086941. doi:10.1029/2019GL086941

Zhang, G., Guo, A., Wang, Y., Li, S., Dong, Y., Liu, S., et al. (2013a). Tectonics of South China continent and its implications. *Sci. China Earth Sci.* 56, 1804–1828. doi:10.1007/s11430-013-4679-1

Zhang, L., Jin, S., Wei, W., Ye, G., Jing, J., Dong, H., et al. (2015a). Lithospheric electrical structure of South China imaged by magnetotelluric data and its tectonic implications. *J. Asian Earth Sci.* 98, 178–187. doi:10.1016/j.jseaes.2014.10.034

Zhang, M., Xu, T., Lü, Q., Bai, Z., Wu, C., Wu, Z., et al. (2015b). 3D Moho depth beneath the middle-lower Yangtze metallogenic belt and its surrounding areas: Insight from the wide angle seismic data. *Chin. J. Geophys.* 58 (12), 4360–4372. doi:10.6038/cjg20151203

Zhang, Y., Cen, L., Ai, Y., Jiang, M., Xu, W., and Shen, Z. (2018). Lithospheric structure of the South China block from S-receiver function. *Chin. J. Geophys.* 61 (1), 138–149. doi:10.6038/cjg2018L0226

Zhang, Y., Dong, S., Li, J., Cui, J., Shi, W., and Su, J. (2012). The new progress in the study of mesozoic tectonics of SouthSouth China. *Acta Geosci. Sin.* 33 (03), 257–279. doi:10.3975/cagsb.2012.03.01

Zhang, Y., Shi, D., Lü, Q., Xu, Y., Xu, Z., Yan, J., et al. (2021). The crustal thickness and composition in the eastern South China Block constrained by receiver functions: Implications for the geological setting and metallogenesis. *Ore Geol. Rev.* 130, 103988. doi:10.1016/j.oregeorev.2021. 103988

Zhang, Y., Xu, Y., Yan, J., Xu, Z., and Zhao, J. (2019a). Crustal thickness, and its relations to mineralization in the southeastern part of South China: Constraint from the teleseismic receiver functions. *Geol. China* 46 (4), 723–736. doi:10.12029/ gc20190404

Zhang, Y. Y., Fang, H., Qiu, G. G., Ai, Y. S., and Zhao, L. (2019b). The lithospheric structure of the lower Yangtze craton and its adjacent regions by S receiver function imaging. *Geol. China* 46 (4), 786–794. doi:10.12029/ gc20190409

Zhang, Z., Badal, J., Li, Y., Chen, Y., Yang, L., and Teng, J. (2005). Crust–upper mantle seismic velocity structure across Southeastern China. *Tectonophysics* 395 (1-2), 137–157. doi:10.1016/j.tecto.2004.08.008

Zhang, Z., Xu, T., Zhao, B., and Badal, J. (2013b). Systematic variations in seismic velocity and reflection in the crust of Cathaysia: New constraints on intraplate orogeny in the South China continent. *Gondwana Res.* 24 (3-4), 902–917. doi:10. 1016/j.gr.2012.05.018

Zhao, J., Zhou, M., Yan, D., Zheng, J., and Li, J. (2011). Reappraisal of the ages of neoproterozoic strata in SouthSouth China: No connection with the grenvillian orogeny. *Geology* 39 (4), 299–302. doi:10.1130/G31701.1

Zhao, K., Jiang, S., Chen, W., Chen, P., and Ling, H. (2013). Zircon U–Pb chronology and elemental and Sr–Nd–Hf isotope geochemistry of two triassic A-type granites in SouthSouth China: Implication for petrogenesis and indosinian transtensional tectonism. *Lithos* 160, 292–306. doi:10.1016/j.lithos.2012.11.001

Zheng, Q., Zhu, J., Xuan, R., and Cai, X. (2003). An approach to the crustal velocities in southern China. *Sediment. Geol. Tethyan Geol.* 23 (4), 9–13.

Zheng, X., Ouyang, B., Zhang, D., Yao, Z., Liang, J., and Zheng, J. (2009). Construction of the technical system of data Backup Centre for China Seismograph network and its support to wenchuan earthquake researches. *Chin. J. Geophys. (in Chin.* 52 (5), 657–662. doi:10.1002/cjg2.1387

Zhou, L., Xie, J., Shen, W., Zheng, Y., Yang, Y., Shi, H., et al. (2012). The structure of the crust and uppermost mantle beneath South China from ambient noise and earthquake tomography. *Geophys. J. Int.* 189 (3), 1565–1583. doi:10.1111/j.1365-246X.2012.05423.x

Zhou, X., Sun, T., Shen, W., Shu, L., and Niu, Y. (2006). Petrogenesis of mesozoic granitoids and volcanic rocks in SouthSouth China: A response to tectonic evolution. *Episodes* 29 (1), 26–33. doi:10.18814/epiiugs/2006/v29i1/004

Zhu, L., and Kanamori, H. (2000). Moho depth variation in southern California from teleseismic receiver functions. *J. Geophys. Res.* 105 (B2), 2969–2980. doi:10.1029/1999JB900322